ERDC MP-21-2

Engineer Research and Development Center

US Army Corps
of Engineers®
Engineer Research and
Development Center

ERDC
ENGINEER RESEARCH & DEVELOPMENT CENTER

# Vertical and Slanted Sound Propagation in the Near-Ground Atmosphere

## Amplitude and Phase Fluctuations

Matthew J. Kamrath, Vladimir E. Ostashev, D. Keith Wilson,
Michael J. White, Carl R. Hart, and Anthony Finn

May 2021

ERDC MP-21-2
May 2021

# Vertical and Slanted Sound Propagation in the Near-Ground Atmosphere

## Amplitude and Phase Fluctuations

Matthew J. Kamrath, Vladimir E. Ostashev, D. Keith Wilson, Carl R. Hart

*Cold Regions Research Laboratory*
*U.S. Army Engineer Research and Development Center*
*72 Lyme Road*
*Hanover, NH 03755*

Michael J. White

*Construction Engineering Research Laboratory*
*U.S. Army Engineer Research and Development Center*
*2909 Newmark Drive*
*Champaign, IL 61822*

Anthony Finn

*Defence and Systems Institute*
*University of South Australia*
*Mawson Lakes, SA 5095, Australia*

Final report

Prepared for U.S. Army Corps of Engineers
Washington, DC 20314

Under Project Number T24, PE 61102A, Task number 01

# Abstract

Sound propagation along vertical and slanted paths through the near-ground atmosphere impacts detection and localization of low-altitude sound sources, such as small unmanned aerial vehicles, from ground-based microphone arrays. This article experimentally investigates the amplitude and phase fluctuations of acoustic signals propagating along such paths. The experiment involved nine microphones on three horizontal booms mounted at different heights to a 135-m meteorological tower at the National Wind Technology Center (Boulder, CO). A ground-based loudspeaker was placed at the base of the tower for vertical propagation or 56m from the base of the tower for slanted propagation. Phasor scatterplots qualitatively characterize the amplitude and phase fluctuations of the received signals during different meteorological regimes. The measurements are also compared to a theory describing the log-amplitude and phase variances based on the spectrum of shear and buoyancy driven turbulence near the ground. Generally, the theory correctly predicts the measured log-amplitude variances, which are affected primarily by small-scale, isotropic turbulent eddies. However, the theory overpredicts the measured phase variances, which are affected primarily by large-scale, anisotropic, buoyantly driven eddies. Ground blocking of these large eddies likely explains the overprediction.

# Preface

This research was sponsored by the U.S. Army Corps of Engineers (USACE), Engineer Research and Development Center (ERDC), Geospatial Research and Engineering business area under Project number T24, Program Element 611102A, Task 01.

The work was performed by the Signature Physics Branch of the Research and Engineering Division, U.S. Army Engineer Research and Development Center, Cold Regions Research and Engineering Laboratory (ERDC-CRREL) and by the Ecological Processes Branch of the Installations Division, Construction Engineering Research Laboratory (ERDC-CERL). At the time of publication, Dr. M. Andrew Niccolai was Branch Chief; Dr. George W. Calfas was Acting Division Chief; and Dr. Bert Davis was the Technical Director for ERDC-CRREL; Dr. Chris Rewerts was Branch Chief; Ms. Michelle Hanson was Division Chief; and Dr. Andrew J. Nelson was the Technical Director for ERDC-CERL.

The Deputy Director for ERDC-CRREL was Mr. David Ringelberg and the Director was Dr. Joseph Corriveau. The Acting Deputy Director for ERDC-CERL was Ms. Michelle Hanson and the Acting Director was Dr. Kumar Topudurti.

We would like to thank the NWTC team, including Mr. David Jager, Mr. Jeroen van Dam, and Mr. John Gagnon (ERDC) for their expert support in conducting the experiment. Ms. Michelle Swearingen (ERDC) and Dr. Gregory Lyons (ERDC) also helped in planning the experiment.

This article was originally published online in the *Journal of the Acoustical Society of America* on 26 March 2021.

The Commander of ERDC was COL Teresa A. Schlosser and the Director was Dr. David W. Pittman.

# Vertical and Slanted Sound Propagation in the Near-Ground Atmosphere: Amplitude and Phase Fluctuations

**ABSTRACT:**
Sound propagation along vertical and slanted paths through the near-ground atmosphere impacts detection and localization of low-altitude sound sources, such as small unmanned aerial vehicles, from ground-based microphone arrays. This article experimentally investigates the amplitude and phase fluctuations of acoustic signals propagating along such paths. The experiment involved nine microphones on three horizontal booms mounted at different heights to a 135-m meteorological tower at the National Wind Technology Center (Boulder, CO). A ground-based loudspeaker was placed at the base of the tower for vertical propagation or 56 m from the base of the tower for slanted propagation. Phasor scatterplots qualitatively characterize the amplitude and phase fluctuations of the received signals during different meteorological regimes. The measurements are also compared to a theory describing the log-amplitude and phase variances based on the spectrum of shear and buoyancy driven turbulence near the ground. Generally, the theory correctly predicts the measured log-amplitude variances, which are affected primarily by small-scale, isotropic turbulent eddies. However, the theory overpredicts the measured phase variances, which are affected primarily by large-scale, anisotropic, buoyantly driven eddies. Ground blocking of these large eddies likely explains the overprediction.

## I. INTRODUCTION

Previous research on sound propagation through the near-ground atmosphere (which refers, here, to altitudes up to roughly a couple hundred meters above ground level) has typically concentrated on nearly horizontal transmission paths.[1–4] However, vertical and slanted transmission paths through the near-ground atmosphere are increasingly important for a variety of timely applications, including acoustic detection and localization of small unmanned aerial vehicles (UAVs) using ground-based microphone arrays[5,6] and acoustic sensing from microphone arrays on UAVs and tethered balloons.[7]

The phenomenology affecting these opposing transmission geometries differ somewhat. Horizontal propagation, which has been well studied, is significantly impacted by geometrical spreading, atmospheric absorption, reflection, refraction, diffraction, and turbulent scattering. In contrast, relatively few studies have focused on vertical and slanted propagation. Some such studies mentioned here include applications to low-flying aircraft,[8] a sound source on a 150-m tower,[9] sonic boom propagation,[10–12] and auralization of flying aircraft.[13] Ostashev and Wilson[14] provide an additional review of this subject. Vertical and slanted paths are mainly impacted by geometrical spreading, atmospheric absorption, and turbulent scattering, whereas factors such as refraction and diffraction typically play a lesser role at least for near-ground geometries.

Geometrical spreading and sound absorption in the lower atmosphere, whether along horizontal or vertical transmission paths, are well understood and can be readily assessed, e.g., Ref. 15. This leaves turbulent scattering as a phenomenon which is poorly understood for vertical transmission geometries in the near-ground atmosphere. Among other effects, atmospheric turbulence causes the amplitude and phase of acoustic signals to fluctuate. This article presents results from a uniquely comprehensive experiment involving vertical and slanted propagation through a turbulent atmosphere and compares the measured variances of the log-amplitude and phase fluctuations to existing theory.

The experiment was conducted in September of 2018 at the National Wind Technology Center (NWTC) of the National Renewable Energy Laboratory (NREL), located near Boulder, CO. The present article details the experimental setup, transmitted acoustic signal forms, meteorological data descriptions, and phasor scatterplots which qualitatively characterize the amplitude and phase fluctuations.

Determination of the turbulence parameters and the log-amplitude and phase variances is performed over the same time interval of about 30 minutes, which enables us to capture the effect of turbulence across all pertinent time scales. In previous studies, the averaging time intervals were usually shorter and, thus, did not address the impact of turbulence on time scales of a minute and longer.

The theory against which we compare the measured log-amplitude and phase variances comes from Ref. 14, which derived the variances for vertical and slanted paths for the height-dependent turbulence model presented in Ref. 3. Another goal of this article is to validate the turbulence model and propagation theory, which are important in many applications. The well-designed NWTC experiment is particularly useful for this purpose because acoustic signals were mainly affected by turbulence rather than by other factors, e.g., interaction with the ground.

This article is organized as follows. Section II provides the geometry of the problem, theoretical formulations for the variances of the log-amplitude and phase fluctuations, and the turbulence model. Section III describes the experiment conducted at the NWTC and pertinent signal processing. Section IV presents the experimental results for the meteorological data, the log-amplitude and phase fluctuations, their variances, and a comparison to the theoretical predictions. Last, Sec. V summarizes the results.

## II. THEORY

### A. Problem formulation

In the NWTC experiment, microphones were placed on a 135-m tower. The sound source was either at the base of the tower for vertical propagation or at some distance from it for slanted propagation. Figure 1 schematically depicts the slanted geometry. Three microphones were located on a horizontal boom mounted to the tower at the height $h$ above the ground. In the vertical $xz$-plane, the propagation path from the source on the ground to the geometrical center $O$ of the microphones has length $L = h/\cos\theta$, where $\theta$ is the angle between the path and the vertical axis.

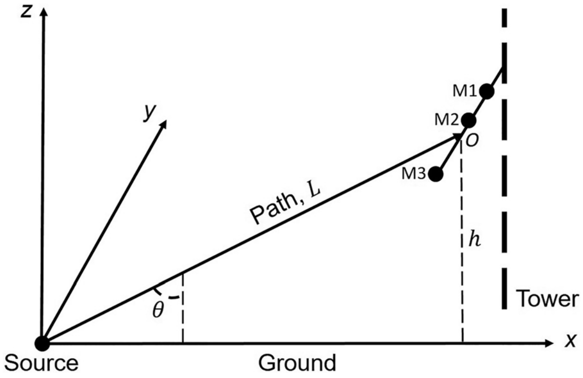

FIG. 1. Geometry for slanted propagation. A loudspeaker on the ground emits sound toward microphones at locations M1, M2, and M3 on a horizontal boom mounted to a tower. $O$ is the geometrical center of the three microphones. The propagation path is in the vertical $xz$-plane.

In the NWTC experiment, the path length $L$ was much greater than the distance between the three microphones. Therefore, the path length and propagation angle to each microphone can be approximated, respectively, as $L$ and $\theta$. In addition, the experiment used three horizontal microphone booms mounted to the tower at different heights $h$, and Fig. 1 only depicts one of them.

Let $p(L,t)$ be the sound pressure at a microphone location where $t$ is time. The sound pressure is affected by temperature and wind velocity fluctuations in a volume encompassing the propagation path. In the quasi-static approximation (e.g., Sec. 2.4.2 in Ref. 3 and Refs. 16 and 17), the sound pressure can be written as

$$p(L,t) = \int_{-\infty}^{\infty} \exp(-i\omega t)\hat{p}(L,\omega,t)\,d\omega, \tag{1}$$

where $\omega$ is the angular sound frequency. In Eq. (1), $\hat{p}(L,\omega,t)$ is the time-varying Fourier transform. The time dependence arises from the temperature and wind velocity fluctuations. Because the characteristic time $T_{\text{tur}}$ of these fluctuations is often much greater than $2\pi/\omega$, $\hat{p}(L,\omega,t)$ varies in time much slower than $\exp(-i\omega t)$. The quantity $\hat{p}(L,\omega,t)$ can be obtained by windowing the measured sound pressure and applying a Fourier transform to each window. The window must be much longer than $2\pi/\omega$ but shorter than $T_{\text{tur}}$; the argument $t$ corresponds to a particular window of time. If a signal comprises a set of tones (as was the case in the NWTC experiment; Sec. III), $\hat{p}(L,\omega,t)$ can also be obtained by bandpass filtering, Hilbert transforming, and complex demodulating each tone.

In the presence of turbulent scattering, both the sound pressure and its transform are random functions. Our goal is to experimentally investigate the log-amplitude and phase fluctuations of $\hat{p}(L,\omega,t)$ with comparisons to existing theoretical predictions. This comparison helps both validate the theory and identify theoretical shortcomings.

### B. Log-amplitude and phase fluctuations

The Rytov method (e.g., Refs. 3 and 18) expresses the sound-pressure transform $\hat{p}(L,\omega,t)$ as

$$\hat{p} = \hat{p}_0 \exp(\chi + i\phi). \tag{2}$$

Here, $\hat{p}_0$ is the transform in a nonturbulent atmosphere, and $\chi(L,\omega,t)$ and $\phi(L,\omega,t)$ are, respectively, the log-amplitude and phase fluctuations due to atmospheric turbulence.

The variance of the log-amplitude fluctuations is defined as

$$\sigma_\chi^2 = \langle \chi^2(L,\omega,t)\rangle, \tag{3}$$

where the brackets $\langle\,\rangle$ denote averaging over an ensemble of turbulence realizations. The variance of the phase fluctuations, $\sigma_\phi^2$, is defined similarly. Assuming statistical stationarity, $\sigma_\chi^2$ and $\sigma_\phi^2$ do not depend on $t$.

In Eq. (78) of Ref. 14, Ostashev and Wilson give the correlation functions of the log-amplitude and phase fluctuations of a spherical sound wave in the Markov approximation for vertical and slanted propagation in statistically inhomogeneous turbulence. Setting the sensor separation to zero in this equation yields the log-amplitude and phase variances,

$$\sigma^2_{\chi,\phi} = \frac{\pi^2 k^2}{2\cos\theta}\int_0^h dz \int_0^\infty \Phi_{\mathrm{eff}}(z,\kappa) \times \left[1 \mp \cos\left(\frac{z(h-z)\kappa^2}{kh\cos\theta}\right)\right]\kappa\, d\kappa. \tag{4}$$

Here, $\sigma^2_\chi$ and $\sigma^2_\phi$ correspond to the upper and lower signs in the square brackets, respectively; $k = \omega/c_0$ is the acoustic wavenumber where $c_0$ is the reference sound speed; and the integration variables are the turbulence wavenumber $\kappa$ and the height along the path $z$. In Eq. (7.30) of Ref. 3, Ostashev and Wilson give the effective turbulence spectrum $\Phi_{\mathrm{eff}}(z,\kappa)$ for the von Kármán spectra of temperature and wind velocity fluctuations,

$$\Phi_{\mathrm{eff}}(z,\kappa) = \frac{\Gamma(11/6)}{\pi^{3/2}\Gamma(1/3)}\left[\frac{\sigma^2_T(z)L^3_T(z)}{T_0^2\left(1+\kappa^2 L^2_T(z)\right)^{11/6}} + \frac{22}{3}\frac{\sigma^2_{v,s}L^5_{v,s}(z)\kappa^2}{c_0^2\left(1+\kappa^2 L^2_{v,s}(z)\right)^{17/6}} + \frac{22}{3}\frac{\sigma^2_{v,b}L^5_{v,b}\kappa^2}{c_0^2\left(1+\kappa^2 L^2_{v,b}\right)^{17/6}}\right]. \tag{5}$$

In this formula, $\Gamma$ is the gamma function; $T_0$ is the reference temperature; $\sigma^2_T$, $\sigma^2_{v,s}$, and $\sigma^2_{v,b}$ are the variances of the temperature fluctuations and the shear- and buoyancy-produced velocity fluctuations, respectively; and $L_T$, $L_{v,s}$, and $L_{v,b}$ are the length scales of the corresponding fluctuations.

In Sec. 6.2.4 of Ref. 3, Ostashev and Wilson present a turbulence model for atmospheric acoustics. Using the mixed-layer and Monin-Obukhov similarity theories, the variances and length scales in the atmospheric boundary layer (ABL) are expressed in terms of the friction velocity ($u_*$), the height above the ground ($z$), and the ABL height ($z_i$). The variances of the temperature fluctuations and the shear- and buoyancy-produced velocity fluctuations are

$$\sigma^2_T(z) = \frac{4.0 T^2_*}{(1-10z/L_o)^{2/3}}, \quad \sigma^2_{v,s} = 3.0 u^2_*, \quad \sigma^2_{v,b} = 0.35 w^2_*, \tag{6}$$

and the corresponding length scales are

$$L_T(z) = 2.0\, z\frac{(1-7z/L_o)}{(1-10z/L_o)}, \quad L_{v,s}(z) = 1.8\, z, \quad L_{v,b} = 0.23\, z_i. \tag{7}$$

Here, $T_* = -\langle w'T'\rangle/u_*$ is the surface-layer temperature scale, $L_o = -u^3_* T_0/(g\kappa_v\langle w'T'\rangle)$ is the Obukhov length, and $w_* = \sqrt[3]{g z_i \langle w'T'\rangle/T_0}$ is the mixed-layer velocity scale. In these formulas, $g = 9.81\ \mathrm{m/s^2}$ is the gravitational acceleration, and $\kappa_v = 0.40$ is the von Kármán constant. The formulas also use the covariance, $\langle w'T'\rangle$, of the vertical wind velocity fluctuations ($w'$) and the temperature fluctuations ($T'$). This turbulence model is valid for an unstable or neutral ABL for which $\langle w'T'\rangle \geq 0$. In some cases, it can also be used for a weakly stable ABL (for which $\langle w'T'\rangle < 0$) by setting $\langle w'T'\rangle = 0$.

No available spectral model captures all the complexities of the atmospheric turbulence. The present model is an improvement over those previously employed in atmospheric acoustics, most notably because it incorporates turbulence produced by both shear and buoyancy instabilities. However, some limiting assumptions should be kept in mind. First, it is formulated for a stationary ABL with well-developed (continuous) turbulence, which is necessary for applying the turbulence similarity theories. Applicability to intermittent turbulent activity and transitional meteorological conditions is, thus, questionable. Second, the model assumes isotropic turbulence. This assumption is justified in the inertial subrange of turbulence where the eddies are isotropic and smaller than the outer scales of temperature and wind velocity fluctuations, which are on the order of the length scales $L_T(z)$, $L_{v,s}(z)$, and $L_{v,b}$. The largest eddies are on the order of these scales and are anisotropic. Third, the model predicts that $L_{v,b}$ in Eq. (7) does not depend on $z$. This assumption is unrealistic because the ground blocks the vertical movement of the air, thus, making the structure of the large eddies anisotropic. In other words, Eqs. (6) and (7) for $\sigma^2_{v,b}$ and $L_{v,b}$ may be valid only for $z \gtrsim L_{v,b} = 023 z_i$. Smaller heights require a more realistic anisotropic turbulence model. Although such a model is beyond the scope of this study, we speculate that Eqs. (6) and (7) could still be used in the horizontal direction, but $\sigma^2_{v,b}$ and $L_{v,b}$ should decrease (e.g., linearly) with the height for $z < 023 z_i$ in the vertical direction. Whereas some previous research has extended turbulence spectral models to incorporate ground blocking,[19,20] they are involved and would need to be adapted for calculating the variances of the log-amplitude and phase fluctuations.

Thus, the theoretical predictions for the log-amplitude and phase variances based on Eq. (4) and the turbulence model, Eqs. (5)–(7), may agree with the experimental results only for certain meteorological regimes and when these variances are primarily affected by isotropic turbulence. Because small-scale turbulence (which is statistically isotropic) affects the log-amplitude fluctuations (e.g., Sec. 7.2.3 in Ref. 3 and Ref. 18), they usually satisfy the isotropic turbulence condition. However, large atmospheric eddies (which are anisotropic) cause phase fluctuations, invalidating the current turbulence model near the ground and requiring a more realistic model to predict these fluctuations. Because such a model has not yet been developed, Eqs. (5)–(7) will be used to predict the phase variance, understanding their limitations. In addition, the log-amplitude and phase variances will be calculated using Eqs. (5)–(7) in which the buoyancy-produced velocity fluctuations are omitted, i.e., $\sigma_{v,b}^2 = 0$. This simplification of the turbulence model helps illuminate the impact of neglecting the buoyancy-produced velocity fluctuations.

Finally, the Markov approximation is only valid when the propagation range is much longer than the scale of the largest eddies affecting the sound field. Therefore, for atmospheric sound propagation, this approximation is usually valid for the log-amplitude variance but may not be valid for the phase variance when the range is not much greater than $L_{v,b}$.[21] Along the propagation paths considered in our near-ground experiment, the scales of the largest eddies are probably smaller than $L_{v,b}$. If this is the case, then the phase variance may be calculated with the Markov approximation. This assumption needs to be revisited after the largest anisotropic eddies and their blocking by the ground are incorporated into the turbulence model.

## III. EXPERIMENTAL METHODS

### A. Experimental setup

A sound propagation experiment was conducted 25–28 September 2018 at the NWTC (Boulder, CO; Ref. 22), situated about 5 km to the east of the Front Range of the Rocky Mountains (Fig. 2). Near Boulder, the Front Range runs north-south. The terrain is flat with short-to-medium grass.

The experiment involved the 135-m meteorological tower shown in Fig. 2. For the prevailing wind direction (from the west-northwest), the tower is upwind of the wind turbines. The horizontal cross section of the tower is an equilateral triangle with a side length of 1.13 m. Nine microphones were installed on three horizontal booms mounted to the tower. Each boom carried three GRAS 40AE 1/2 in. prepolarized free-field microphones (Holte, Denmark). The microphones had windscreens and water-resistant shrouds and were positioned upward (Fig. 3). The distances between the microphones and the tower were 0.5 m, 1.3 m, and 2.8 m; the geometrical center $O$ of the microphones (Fig. 1) was 1.5 m from the tower. The microphone booms were mounted to the tower at the heights 39 m, 80 m, and 130 m above the ground. The microphone booms pointed toward north-northwest (338°). In this article, the conventional cardinal directions are used: north corresponds to 0° (or 360°) and the azimuth angle $\psi$ increases clockwise. The tower has 18 horizontal booms with meteorological instruments (Fig. 2) mounted to the tower at various heights; these booms point west (278°).

FIG. 3. (Color online) Microphone and meteorological booms attached to the tower (view from the tower towards the ground).

FIG. 2. (Color online) NWTC in the foothills of the Rocky Mountains. The experiment used the red and white tower on the right. [Credit: Dennis Schroeder, National Renewable Energy Lab, Department of Energy (DOE, Washington, DC)].

The acoustic source consisted of an EM280 driver and PC364 horn (Community Professional Loudspeakers, Chester, PA). For the sound frequency $f = \omega/(2\pi) = 2\,\mathrm{kHz}$, the beam widths (defined by 6 dB attenuation from the maximum transmitted power) in two perpendicular directions are 45° and 50°, respectively; the beam widths are frequency dependent. In the vertical sound propagation trials, the ground-based source was 3.7 m from the tower along the projection of the microphone booms on the ground, and the horn aperture was 0.53 m above the ground pointing straight up. This setup minimized the sound reflection from the ground. Two reference microphones (GRAS 40AE ½ in. microphones, Holte, Denmark) were positioned near the source within the beam widths. Some transmissions used a horn PC394F (Community Professional Loudspeakers, Chester, PA), which had a slightly wider beam width.

In the slanted propagation trials, the angle between the horn axis and vertical was 14.9°. In this case, reflections from the ground were minimal, and all microphones on the tower were still insonified. Figure 4 depicts the geometry of slanted propagation in the horizontal plane. The $x$ axis coincides with the projection of the propagation path, depicted in Fig. 1, on the ground; the $x$- and $y$ axes are the same in

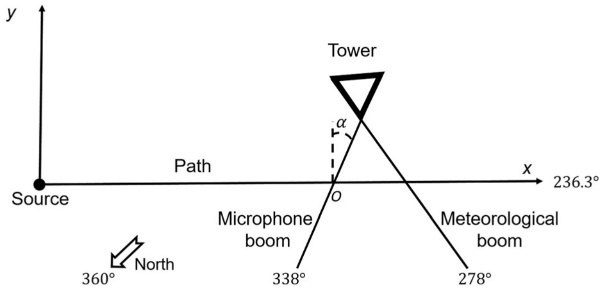

FIG. 4. Plan view of slanted sound propagation in the horizontal plane. The equilateral triangle represents the tower, and the microphone and meteorological booms are mounted to two sides of the tower. In the figure, $O$ is the geometrical center of the microphones.

both Figs. 1 and 4. In the experiment, the $x$ axis pointed in the direction of 236.3°. The angle $\alpha = 11.7^\circ$ characterizes the angle between the $y$ axis and the microphone boom. The geometry would have been simpler if $\alpha = 0^\circ$; however, in that case, the propagation path would have been too close to a tower guy-wire, which was undesirable.

For slanted propagation, the speaker was 56.0 m from the projection of the geometrical center $O$ of the microphones on the ground. Analysis of Fig. 1 for heights 39 m, 80 m, and 130 m reveals the path lengths $L$ to the three booms were 68.2 m, 97.7 m, and 141.5 m; and the propagation angles $\theta$ were 55.1°, 35.0°, and 23.3°, respectively.

Acoustic signals were prerecorded on a compact disc (CD) player (HD/CD CDR420, Marantz Professional, Cumberland, RI) with a sampling rate of 44.1 kHz and transmitted during the experiment via a power amplifier and the acoustic source. Outputs of the CD player, 9 microphones on the tower and 2 reference microphones were recorded by a 16 channel Yokogawa DL750 ScopeCorder data acquisition system (DAQ; Musashino, Tokyo, Japan) with a sampling rate of 20 kHz. To provide synchronization to UTC, an Inter-Range Instrumentation Group (IRIG) code B clock signal from a Global Positioning System (GPS) receiver was also recorded on one channel of the DAQ. The CD player, DAQ, and power amplifier were located in a truck parked at the base of the tower.

Two continuous waveforms were transmitted: 12 tones and 9 tones. Using 100 Hz increments, the 12 tones had frequencies of 0.6–0.9, 1.4–1.7, and 3.2–3.5 kHz. The nine tones excluded frequencies 0.9, 1.7, and 3.5 kHz. Transmission sequences were either 20 or 40 minutes in duration. Sixteen sequences of tones were recorded successfully. Background noise was recorded. Short chirps were also transmitted and will be used in future work.

### B. Impermissible wind directions

The meteorological and acoustic measurements may be invalid when the instruments or the propagation path are in the wake of the tower, which distorts the measurements. For the meteorological measurements, Sadoud[23] provides the tower wake analysis for instruments at the end of the 3.7- and 7.3-m booms. Interpolating these results for the 6.1-m booms used in this experiment yields the impermissible wind directions: $80.4^\circ < \psi < 114.5^\circ$. (Here, $\psi$ is the direction from which the wind is blowing.)

For the acoustic measurements, the microphones were too close to the tower to interpolate Sadoud's results. Instead, this section uses the geometrical "shadow" of the tower, i.e., the region in the horizontal plane that is covered by horizontal lines with certain angles $\psi$ which pass through the tower. Figure 4 indicates that the microphones are in the tower geometrical shadow for winds from $338^\circ + 120^\circ - 360^\circ = 98^\circ < \psi < 338^\circ - 180^\circ = 158^\circ$. The tower wake is somewhat larger than the geometrical shadow, therefore, choosing an approximate buffer angle of $\Delta\psi_1 = 30^\circ$ yields $68^\circ < \psi < 188^\circ$. This constraint is more restrictive than the constraint for the meteorological booms.

Finally, the sound propagation path should not be in the tower wake. Because the angular position of the vertical propagation path is the same as that of the microphones, this path does not further restrict the allowable wind directions. Thus, for vertical propagation, the impermissible wind directions were

$$68^\circ < \psi < 188^\circ. \tag{8}$$

For slanted propagation, the tower geometrical shadow overlapped with the propagation path for wind directions $132.6^\circ < \psi < 234.8^\circ$. Accounting for the buffer angles $\Delta\psi_2$ and $\Delta\psi_3$ produce $132.6^\circ - \Delta\psi_2 < \psi < 234.8^\circ + \Delta\psi_3$. The buffer angles are not the same in this case because they decrease with increasing distance from the tower. The angle $\Delta\psi_2$ is pertinent to the case when the propagation path was close to the tower and can be approximated as $\Delta\psi_2 = \Delta\psi_1 = 30^\circ$. The angle $\Delta\psi_3$ is pertinent to the case when the propagation path was about 50 m from the tower; let $\Delta\psi_1 = 10^\circ$. (At 7.3 m from the tower, Sadoud[23] estimates that this angle is 15°.) These buffer angles for the propagation path result in $102.6^\circ < \psi < 235.8^\circ$. Combining all of the constraints yields the impermissible wind directions for the slanted propagation

$$68^\circ < \psi < 235.8^\circ. \tag{9}$$

### C. Meteorological data

The NWTC provided the raw and preprocessed data (all synchronized to UTC) for all meteorological instruments installed on the 135-m tower. For the six ATI Model K sonic anemometers (Applied Technologies Inc., Longmont, CO) with a sampling rate of 20 Hz, the NWTC preprocessed the data by removing the invalid data from the raw time series, de-noising data to remove spikes, and remapping the data to a regular time base. We calculated the streamwise ($u$), lateral ($v$), and vertical ($w$) wind velocities over each measurement period. Detrending the anemometer data produced the streamwise ($u'$), lateral ($v'$), and vertical ($w'$) wind velocity fluctuations used to calculate the friction velocity

$$u_* = \left( \langle u'w' \rangle_{t_r}^2 + \langle v'w' \rangle_{t_r}^2 \right)^{1/4}. \tag{10}$$

Here, $\langle \rangle_{t_r}$ stands for averaging over the time interval $t_r$ of an acoustic recording. The surface sensible heat flux, which is proportional to the covariance term $\langle w'T' \rangle$ in $T_*$, $L_o$, and $w_*$ is

$$Q_H = \varrho_a C_p \langle w'T' \rangle_{t_r}. \tag{11}$$

Here, $C_p = 1.01\ \mathrm{J\,g^{-1}\,K^{-1}}$ is the specific heat of air at constant pressure and $T'$ is the temperature fluctuation measured by a sonic anemometer and obtained similarly to the velocity fluctuations.

All six sonic anemometers were used to obtain the vertical profile of the wind speed and its direction, $\psi$. The temperature $T_0$ was measured with a temperature probe, and the atmospheric pressure $P$ was measured with a barometer, both at the height of 3 m above the ground. The air density was then calculated as $\varrho_a = P/(R_a T_0)$, where $R_a = 287\,\text{m}^2/(\text{s}^2\,\text{K})$ is the gas constant for dry air.

The momentum and sensible heat fluxes can be used to calculate the flux Richardson number,[24] which indicates the tendency of the flow to become or remain turbulent. The flux Richardson number is defined as

$$R_f = \frac{(g/T_0)\langle w'T'\rangle}{\langle u'w'\rangle(\partial\langle u\rangle/\partial z) + \langle v'w'\rangle(\partial\langle v\rangle/\partial z)}. \tag{12}$$

When $R_f < 1$ (including negative values), the flow is generally turbulent. When $R_f > 1$, turbulence tends to decay.

The ABL height was not measured but set to $z_i = 1$ km, which is typical for the NWTC site during daytime.[24] The height $z_i$ and meteorological measurements described in this subsection are sufficient to calculate the variances and length scales of the temperature and wind velocity fluctuations needed for predictions of the log-amplitude and phase variances (Sec. II B).

### D. Signal processing

The signals from each microphone and from the CD player were bandpass filtered near each transmitted tone to separate the tones and reduce noise. The bandpass filter was a 7–9 order Butterworth filter designed to have a 10 Hz bandwidth, 0.001 dB maximum passband ripple, and 40 dB attenuation stop band beginning 100 Hz from the center frequency. The passband filter was applied to the signal in forward and reverse time order so as to remove the filter phase delay in the passband and to double the stop band attenuation.

Post-analysis revealed that the CD player, unfortunately, generated a phase discontinuity after playing for approximately 30 minutes. Therefore, all recordings were truncated immediately prior to this phase jump. Post-analysis also revealed that the CD player's clock ran slightly fast so that the instantaneous frequencies were all slightly above their nominal values in each band. For example, for the trial on 09/26 at 11:02, the 3400 Hz band had a median instantaneous frequency of 3400.4444 Hz and a clock slew of 130.70 ppm. For each recording, the clock slew was estimated using the guide band (3400 Hz) from the CD player and that value of clock slew was applied to determine all tone frequencies $\omega_{\text{tr}}$ that were transmitted by the CD player. The 3400 Hz band was the guide band because it was the highest band included in both the 9- and 12-tone transmissions.

After bandpass filtering, the Hilbert transform was applied to convert the real signals at each microphone to complex signals. Then, the signal was complex demodulated to remove the carrier frequency, i.e., the signal was multiplied by $\exp(i\omega_{\text{tr}} t)$. The resulting bandpass filtered, Hilbert transformed, and complex demodulated signal at a microphone corresponds to the sound-pressure transform $\hat{p}$ in Eqs. (1) and (2).

## IV. EXPERIMENTAL AND THEORETICAL RESULTS

### A. Experimental trials and meteorological data

Table I summarizes trial and meteorological information for the 16 tone recordings. The dates and times are specified in the local time zone, which is Mountain Daylight Savings Time (MDT; UTC-06:00). The indicated duration of each trial is the time before the CD player generated a phase discontinuity. The path orientation indicates whether

TABLE I. Trials with 9- or 12-tone recordings, and the meteorological conditions during these trials. The columns indicate the date, local time, usable length of the trial, geometry of the path, number of tones, and meteorological observations at the indicated heights. Values for these observations are the means plus/minus the standard deviations. MDT, Mountain Daylight Savings Time.

| Date (mm/dd) | Time (MDT) | Length (s) | Path | Tones | Wind speed 15 m (m/s) | Wind direction 15 m (°) | Temperature 3 m (°C) | Friction velocity 15 m (m/s) | Sensible heat flux 15 m (W/m$^2$) | Richardson 15–41 m |
|---|---|---|---|---|---|---|---|---|---|---|
| 09/25 | 06:45 | 1808 | Vertical | 12 | 4.4 ± 0.7 | 338 ± 6 | 5.16 ± 0.15 | 0.27 ± 0.07 | −4.2 ± 4.2 | 0.04 |
| 09/25 | 12:45 | 1201 | Vertical | 12 | 3.2 ± 1.4 | 304 ± 25 | 12.41 ± 0.31 | 0.40 ± 0.25 | 290 ± 200 | −2.83 |
| 09/25 | 13:16 | 1201 | Vertical | 12 | 2.5 ± 1.2 | 335 ± 28 | 13.19 ± 0.53 | 0.36 ± 0.22 | 320 ± 180 | −6.08 |
| 09/25 | 13:47 | 1816 | Vertical | 12 | 2.9 ± 1.4 | 312 ± 38 | 13.73 ± 0.38 | 0.35 ± 0.24 | 300 ± 320 | −4.89 |
| 09/25 | 15:44 | 1793 | Vertical | 9 | 3.0 ± 1.0 | 325 ± 30 | 14.59 ± 0.22 | 0.35 ± 0.17 | 170 ± 98 | −3.01 |
| 09/26 | 09:59 | 1783 | Vertical | 9 | 3.2 ± 0.9 | 326 ± 18 | 11.93 ± 0.21 | 0.25 ± 0.13 | 190 ± 100 | −6.83 |
| 09/26 | 11:02 | 1832 | Vertical | 12 | 2.5 ± 1.0 | 303 ± 27 | 13.59 ± 0.25 | 0.31 ± 0.17 | 180 ± 130 | −4.56 |
| 09/27 | 09:06 | 1832 | Slanted | 9 | 5.0 ± 1.7 | 126 ± 20 | 18.73 ± 0.19 | 0.60 ± 0.23 | 88 ± 61 | −0.20 |
| 09/27 | 10:01 | 1824 | Slanted | 12 | 4.8 ± 1.7 | 94 ± 51 | 20.16 ± 0.52 | 0.79 ± 0.37 | 130 ± 130 | −0.33 |
| 09/27 | 12:48 | 1723 | Slanted | 9 | 5.3 ± 1.3 | 308 ± 18 | 21.70 ± 0.28 | 0.41 ± 0.16 | 140 ± 93 | −1.54 |
| 09/27 | 13:41 | 1826 | Slanted | 9 | 4.5 ± 1.3 | 290 ± 21 | 22.78 ± 0.28 | 0.32 ± 0.18 | 110 ± 84 | −1.86 |
| 09/27 | 14:35 | 1824 | Slanted | 9 | 3.3 ± 1.3 | 247 ± 25 | 23.38 ± 0.23 | 0.34 ± 0.21 | 140 ± 110 | −3.94 |
| 09/28 | 05:40 | 1825 | Slanted | 9 | 2.8 ± 0.6 | 231 ± 9 | 4.89 ± 0.08 | 0.24 ± 0.07 | 7.4 ± 3.9 | −0.21 |
| 09/28 | 07:35 | 1802 | Slanted | 12 | 1.9 ± 0.5 | 290 ± 17 | 4.61 ± 0.08 | 0.17 ± 0.07 | 13 ± 11 | −2.11 |
| 09/28 | 08:45 | 1801 | Slanted | 9 | 3.0 ± 0.6 | 301 ± 11 | 4.70 ± 0.10 | 0.23 ± 0.11 | 28 ± 29 | −1.42 |
| 09/28 | 10:35 | 1825 | Slanted | 9 | 1.9 ± 0.5 | 315 ± 18 | 5.56 ± 0.11 | 0.14 ± 0.08 | 27 ± 18 | −9.52 |

the sound propagation was vertical or slanted. Seven trials with vertical propagation were conducted on the first two days, while nine trials with slanted propagation were conducted on the last two days.

Most of the wind directions are valid with respect to the tower wake (Sec. III B) except for the first two trials on 09/27 (at 09:06 and 10:01 MDT). The trial on 09/28 at 05:40 MDT also has a borderline invalid wind direction. According to Eq. (9), the wind direction should be larger than 235.8°, but the mean wind direction is 231°. Nevertheless, this trial is of substantial interest because it is the only one occurring entirely before sunrise at around 06:55 MDT.

The temperature and its variability on 09/28 were relatively small compared to similarly timed measurements on the previous days, probably resulting from the increased cloud cover on this day. Based on the photographs taken during the measurements, skies were clear on 09/25–26, partly cloudy on 09/27, and overcast on 09/28.

The friction velocities and sensible heat fluxes in Table I were estimated from the sonic anemometer data at a 15 m height. The means were calculated over the duration of the corresponding trial and the standard deviations using a one-minute moving average. Most of the trials can be characterized as moderately windy and unstable stratification (positive sensible heat flux). The trial on 09/25 at 06:45 was the only one with a negative sensible heat flux, indicating weakly stable stratification. For the trial on 09/27 at 09:06, the wind was relatively strong with a small positive heat flux. Hence, this trial is representative of windy, near-neutral conditions. For the trials on 09/28, the wind speed was relatively low and the temperature profiles were close to neutral because of the cloud cover. These trials span a time period starting before and ending after sunrise and, hence, exemplify a nonstationary situation.

The values of flux Richardson numbers, $R_f$, in Table I were estimated using the wind and temperature measurements at 15 and 41 m. We see that $R_f$ is negative for all trials except for the trial on 09/25 at 06:45. For this trial, although $R_F$ is positive, the condition $R_f < 1$ is still met, therefore, we would expect turbulence to occur but perhaps be weaker than it was in the other trials.

Based on these meteorological characterizations, we examine four example cases in more detail: 09/25 starting at 06:45 for a weakly stable condition with vertical propagation, 09/25 starting at 12:45 for an unstable condition with vertical propagation, 09/27 starting at 12:48 for an unstable condition with slanted propagation, and 09/28 starting at 05:40 for a low-wind, cloudy atmospheric condition with slanted propagation. The unstable conditions may be regarded as typical daytime cases, whereas the weakly stable and cloudy low-wind conditions explore the limits of the theory and demonstrate interesting atmospheric effects. Figures 5–8 show the horizontal wind speed and direction, temperature, friction velocity, and sensible heat flux versus time for each of the four cases. To better distinguish the trends, a 10-s moving average was applied to the temperature and wind velocity, and a one-minute moving average

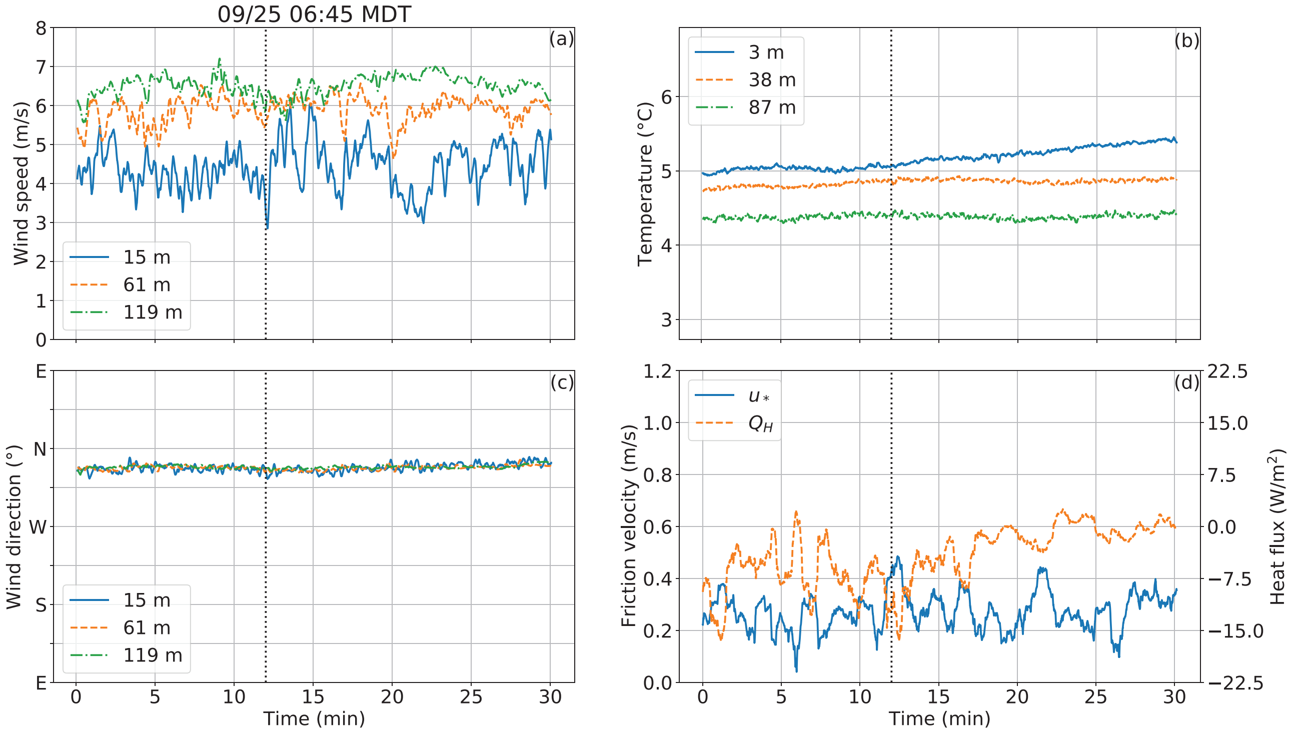

FIG. 5. (Color online) Meteorological time series for the trial on 09/27 at 06:54 (a weakly stable ABL, vertical propagation). (a) illustrates the wind speed at 15 m (blue, solid), 61 m (orange, dashed), and 119 m (green, dashed-dotted) heights; (b) displays the temperature at 3 m (blue, solid), 28 m (orange, dashed), and 87 m (green, dashed-dotted) heights; (c) gives the direction from which the wind is blowing at 15 m (blue, solid), 61 m (orange, dashed), and 119 m (green, dashed-dotted) heights; and (d) provides the friction velocity $u_*$ (blue, solid) and sensible heat flux $Q_H$ (orange, dashed).

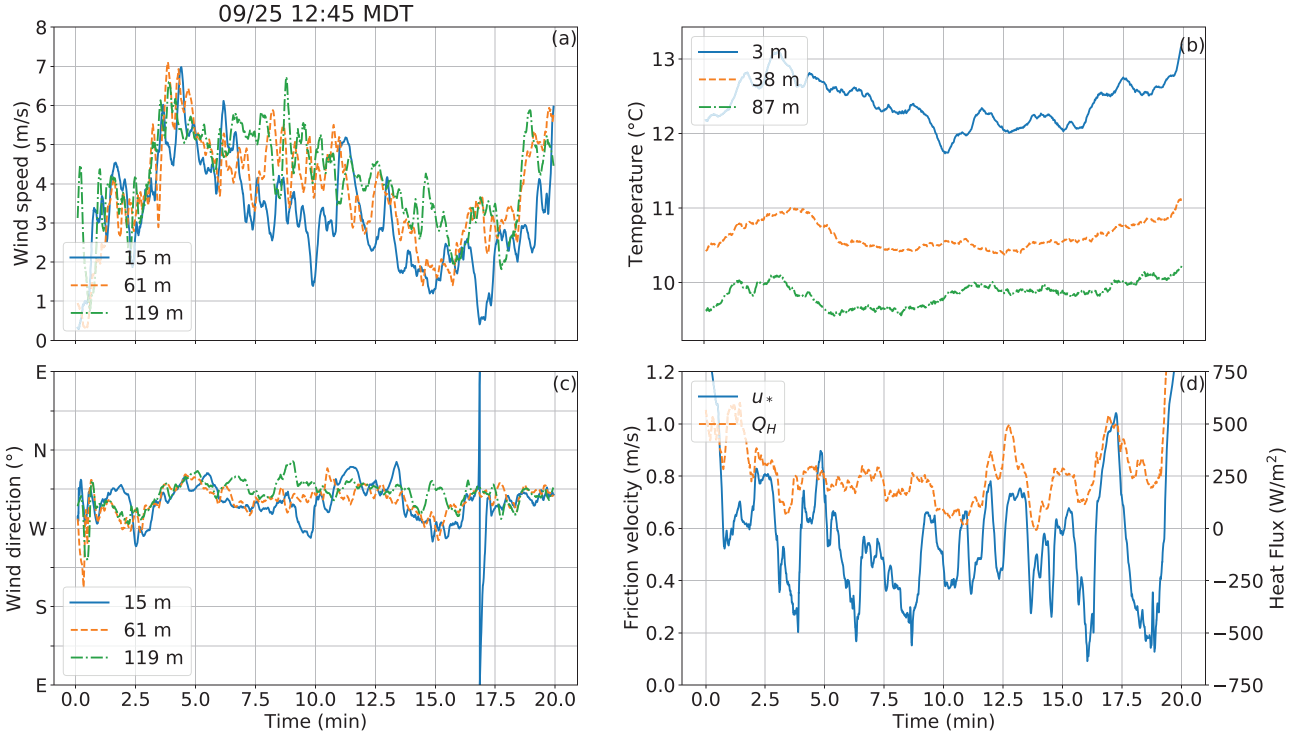

FIG. 6. (Color online) Details are the same as in Fig. 5 but for the trial on 09/25 at 12:45 (an unstable ABL, vertical propagation).

was applied to the friction velocity and surface heat flux. Note the change of scales for the sensible heat flux in Figs. 5 and 8 in comparison to those in Figs. 6 and 7.

For 09/25 at 06:45, shown in Fig. 5, the wind speeds increase with the height while the variability decreases. The temperature at 3 m starts to increase at around 12 min into the trial, whereas the temperatures at the other two heights are steady. Also, around this time, the wind speed at 15 m appears to become more variable. We mark this event in Fig. 5 with a vertical dotted line. Although this transition

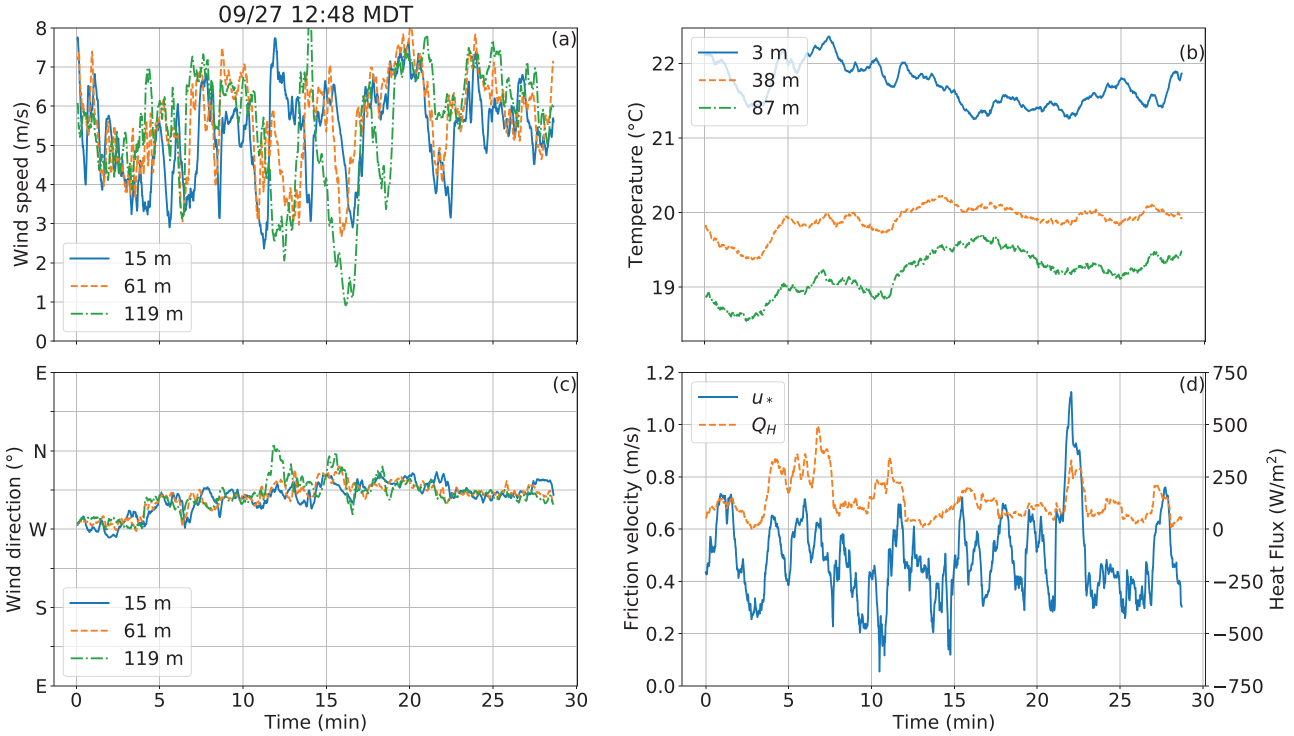

FIG. 7. (Color online) Details are the same as in Fig. 5 but for the trial on 09/27 at 12:48 (an unstable ABL, slanted propagation).

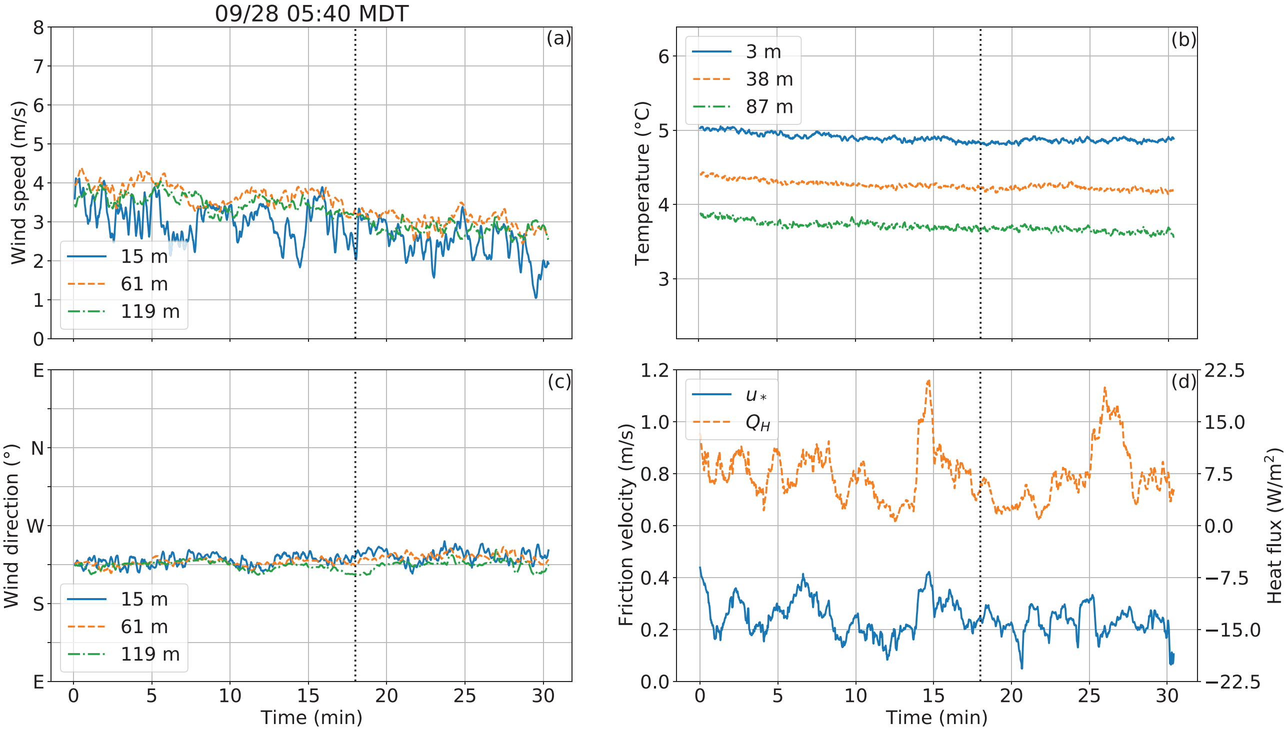

FIG. 8. (Color online) Details are the same as in Fig. 5 but for the trial on 09/28 at 05:40 (low-wind and cloudy, slanted propagation).

occurs around sunrise at 06:55, that may not be the cause of the increasing temperature as the solar radiation is still quite weak around sunrise. Close examination of the wind at 15 m shows events involving wind speeds nearly equal to those at 61 and 119 m; these events suggest that relatively fast moving and warm air aloft is being intermittently mixed downward toward the ground.

For 09/25 at 12:45, shown in Fig. 6, wind speeds are similar at the three observation heights and vary substantially throughout the measurement period on time scales from several seconds to tens of minutes. The temperature gradient near the ground is much more strongly negative than it was earlier in the morning, and the temperatures are more variable, especially at 3 m height. Both the friction velocity and sensible heat flux have much variability as well, and the sensible heat flux is usually a large positive value. The measurements for 09/27 at 12:48, shown in Fig. 7, are qualitatively similar to those in the previous afternoon case.

For 09/28 at 05:50, shown in Fig. 8, the measurements are qualitatively more similar to those in the weakly stable morning case (09/25 at 06:45) than those in the unstable afternoon cases. However, the wind speeds are very similar at all observation heights. The 15 m wind speed has by far the greatest variability, and the 61 m wind speed is often greater than the 119 m wind speed. This behavior may indicate the presence of a low-level jet and stratification of turbulent activity. The temperatures are very stable but slowly decreasing because this measurement finishes about 35 min before sunrise. The temperature differences between the three heights correspond closely to the adiabatic lapse rate of 0.98 °C/100 m. However, at around 18 min into the trial (a vertical dotted line), the temperature at 3 m appears to start warming slightly while the temperature at 87 m continues to cool. This transition will be discussed later because it appears to have a pronounced impact on the signal behavior. The friction velocity and its variability are relatively low, similar to those in the other morning case. The sensible heat flux is small but positive with little variability.

## B. Phasor scatterplots

In this subsection, we consider the behavior of the transformed pressure $\hat{p}$ for the four trials discussed in Sec. IV A. Specifically, we examine the scatterplots of temporal samples of the energy-normalized wavefunction phasor, which is defined as $\hat{\Psi} = \hat{p}/\sqrt{|\hat{p}_0|^2}$, where $\hat{p}_0$ is the unscattered pressure given by Eq. (2). By the conservation of energy, $\langle|\hat{p}|^2\rangle = |\hat{p}_0|^2$. The choice of the normalization factor (the denominator in the definition of $\hat{\Psi}$), thus, ensures that $\langle|\hat{\Psi}|^2\rangle = 1$. As we cannot actually observe the unscattered pressure $\hat{p}_0$, the normalization is performed with $\langle|\hat{p}|^2\rangle$ in lieu of $|\hat{p}_0|^2$. This process loses the phase of $\hat{p}_0$, therefore, the initial phase of $\hat{\Psi}$ is arbitrary.

The phasor scatterplots provide a useful visual depiction of the scattering regime. Amplitude variations (the magnitude of $\Psi$) spread the samples in the radial direction, whereas phase variations (the phase of $\Psi$) spread the samples in angle. When the amplitude and phase variations are both small, as is the case for *unsaturated* scattering, the samples are confined to a small arc on the unit circle. If the amplitude variations are small but the phase variations are large (greater than 360°), then the samples spread around the entire unit circle and create a bull's-eye pattern as is characteristic of the *partial saturation* regime. When the amplitude and phase variations are both large, the center of the unit circle fills in; this behavior is characteristic of the *full saturation* regime. In this regime, the signal undergoes frequent deep fading events, meaning that the amplitude occasionally drops to a value near zero. Because the phase cannot be accurately tracked (i.e., unwrapped) through these deep fading events, the concept of phase variance does not apply to the saturated regime.

Figure 9 shows the phasor scatterplots for the four selected trials. The scatterplots are for the lowest and highest heights (39 and 130 m) and the frequencies 600 and 3400 Hz. These examples span the full spectrum of scattering behavior from unsaturated (e.g., 09/25 at 06:45 at 39 m, 600 Hz), to partially saturated (e.g., 09/27 at 12:48 at 39 m, 600 Hz), and finally to fully saturated (e.g., 09/25 at 12:45 at 130 m, 3400 Hz). For all four trials, the amplitude and phase variations increase with frequency as expected. For three of the cases, the variations increase with height (i.e., length of the propagation path) as expected. However, in the fourth case (09/28 at 05:40), the amplitude and phase variations show a slight tendency to *decrease* with height. This effect is likely due to the slanted propagation path geometries and atmospheric stratification. In this case, the slanted paths do not overlap and the wind speed variability was much higher near the ground (Fig. 8). Thus, the propagation path to the lowest microphones (39 m) may have a larger percentage of the path in more turbulent air, leading to greater signal variations. Because stratification of the turbulence does not

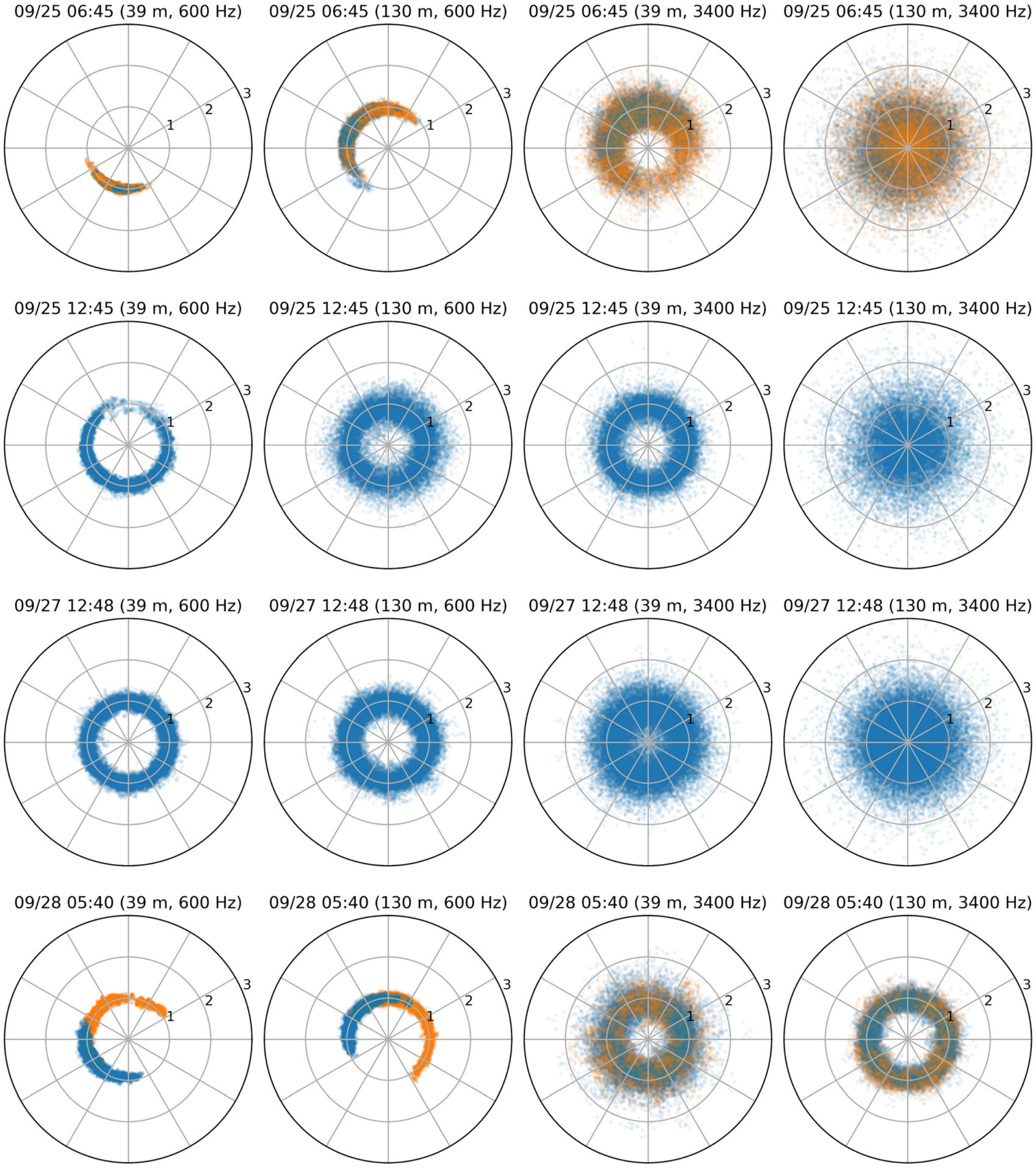

FIG. 9. (Color online) Phasor scatterplots for the four selected trials. Each row presents results for one of the trials obtained at 39 m and 130 m, and for 600 Hz and 3.4 kHz. The rows with two colors show the data before (blue) and after (orange) the vertical dashed lines in Figs. 5 and 8.

generally occur for unstable atmospheric conditions as were present during the other slanted propagation trial (09/27 at 12:48), the variations predictably increased with height for that case.

The amplitude and phase variations also tend to increase as the atmospheric instability (surface sensible heat flux) increases. The weakly stable case (09/25 at 06:45) has the smallest variations, the low-wind cloudy case (09/28 at 05:40) has the next smallest variations, and the two unstable cases have the largest variations. Although the sensible heat flux is larger for the 09/25 at 12:45 vertical propagation case than for the 09/27 at 12:48 slanted propagation case, the variations are slightly larger for the 09/27 at 12:48 case at the 39 m height, in contrast to the established pattern, probably because of the much longer propagation distance for the slanted case.

### C. Time series of log-amplitude and phase fluctuations

This section examines the time series of the fluctuations in the log-amplitude ($\ln|\Psi|$) and unwrapped phase of $\Psi$ for the four previously considered trials. Figure 10 plots the log-amplitude and phase at 39 m height for the frequency of 600 Hz. Again, a 10-s moving average removes the highest frequency fluctuations so that the entire 20–30 min time series can be viewed readily. This plot uses the lowest height and frequency to avoid the saturated regime for which the phase cannot be unwrapped. For present purposes, we consider that the phase cannot be unwrapped if the maximum change in phase between time-adjacent points ($\Delta t = 0.05$ s) exceeds 90°.

For all of the trials, the phase appears to fluctuate over longer time scales than the log-amplitude. This occurs because the eddies affecting the log-amplitude are mostly on the spatial scale of the Fresnel zone, whereas the eddies affecting the phase are the largest eddies in the ABL.

The trial on 09/25 at 06:45 for weakly stable conditions exhibits much smaller log-amplitude fluctuations than the other three trials. The trial on 09/28 at 05:40 for low-wind cloudy conditions exhibits log-amplitude fluctuations similar to the two afternoon cases despite its neutral atmosphere. This may be a result of the high wind speed variability for this trial.

The signal phase for the trial on 09/25 at 06:45 also behaves differently from the other three cases. For this one trial, the phase mostly fluctuates about a fixed value without evidence of a long-term trend. For the other three trials, the phase wanders on a time scale larger than the 20–30 min measurement. Because the largest eddies in the flow tend to drive the signal phase variations, the characteristic sizes of the eddies are apparently smaller for the weakly stable case.

### D. Sound scattering by the tower

For the vertical propagation trials, the signal amplitudes measured by some microphones were affected by the scattering from the tower. This scattering can be qualitatively assessed by considering the first Fresnel zone along the source-microphone propagation path. The first Fresnel zone is a fairly large region in space where the scattered wave is in phase with the unscattered wave from a source to a receiver. Scattering from this region leads to significant amplitude fluctuations. If the tower was within the first Fresnel zone, noticeable scattering is expected. Going beyond the first Fresnel zone, there are alternating regions where the scattering tends to be in phase or out of phase with the unscattered wave. But these regions are smaller in size and scattering from them is often modeled as incoherent. The radius of the first Fresnel zone is given by

$$r_F(z) = \sqrt{\lambda z(1 - z/h)}. \tag{13}$$

Here, $\lambda$ is the sound wavelength, $z$ is the height along the path, and $h$ is the microphone height.

Figure 11 depicts both the Fresnel zone radii (colored curves) and horizontal distances between the tower and the propagation paths (black lines) for the microphones at $h = 39$ m (top subplot) and $h = 130$ m (bottom subplot). Each colored curve gives the Fresnel radius for a different frequency where the lowest frequency has the largest Fresnel radius. Each black line gives the horizontal distance between the propagation path and the tower for a different microphone on the same boom. All black lines start at a source distance from the tower (3.7 m) and end at their microphone locations: 0.5 m (dashed), 1.3 m (dashed-dotted), or 2.8 m (dotted). If a colored curve is above a black line, then the tower is in the first Fresnel zone.

It follows from Fig. 11 that for $h = 39$ m, only the microphone at 2.8 m was not affected by sound scattering by the tower. This was also the case for $h = 130$ m in the 1 kHz and 3 kHz ranges, but not in the 600 Hz range. The results obtained but not presented here show that for $h = 80$ m, the sound scattering by the tower is qualitatively similar to that for $h = 39$ m.

### E. Log-amplitude and phase variances for the four trials

The log-amplitude and phase fluctuations considered in Sec. IV C were detrended and then used to calculate the corresponding variances, $\sigma_\chi^2$ and $\sigma_\phi^2$. The averaging was done over the same time interval as for the meteorological parameters (Sec. III C).

Figure 12 depicts the variance of the log-amplitude fluctuations, $\sigma_\chi^2$, versus frequency, $f$, for the four trials considered in Secs. IV A–IV C. The symbols correspond to the experimental results obtained with the three microphones at the heights $h = 39$ m and 130 m. The dashed lines (marked BST, which stands for buoyancy-shear-temperature) correspond to the theoretical results for $\sigma_\chi^2$, obtained with Eqs. (4)–(7), which will be referred to as the BST predictions. The dashed-dotted lines (marked ST, or shear-temperature) are the same predictions except that the buoyancy-produced velocity fluctuations are set to zero as explained at the end of Sec. II B. These theoretical results are referred to as the

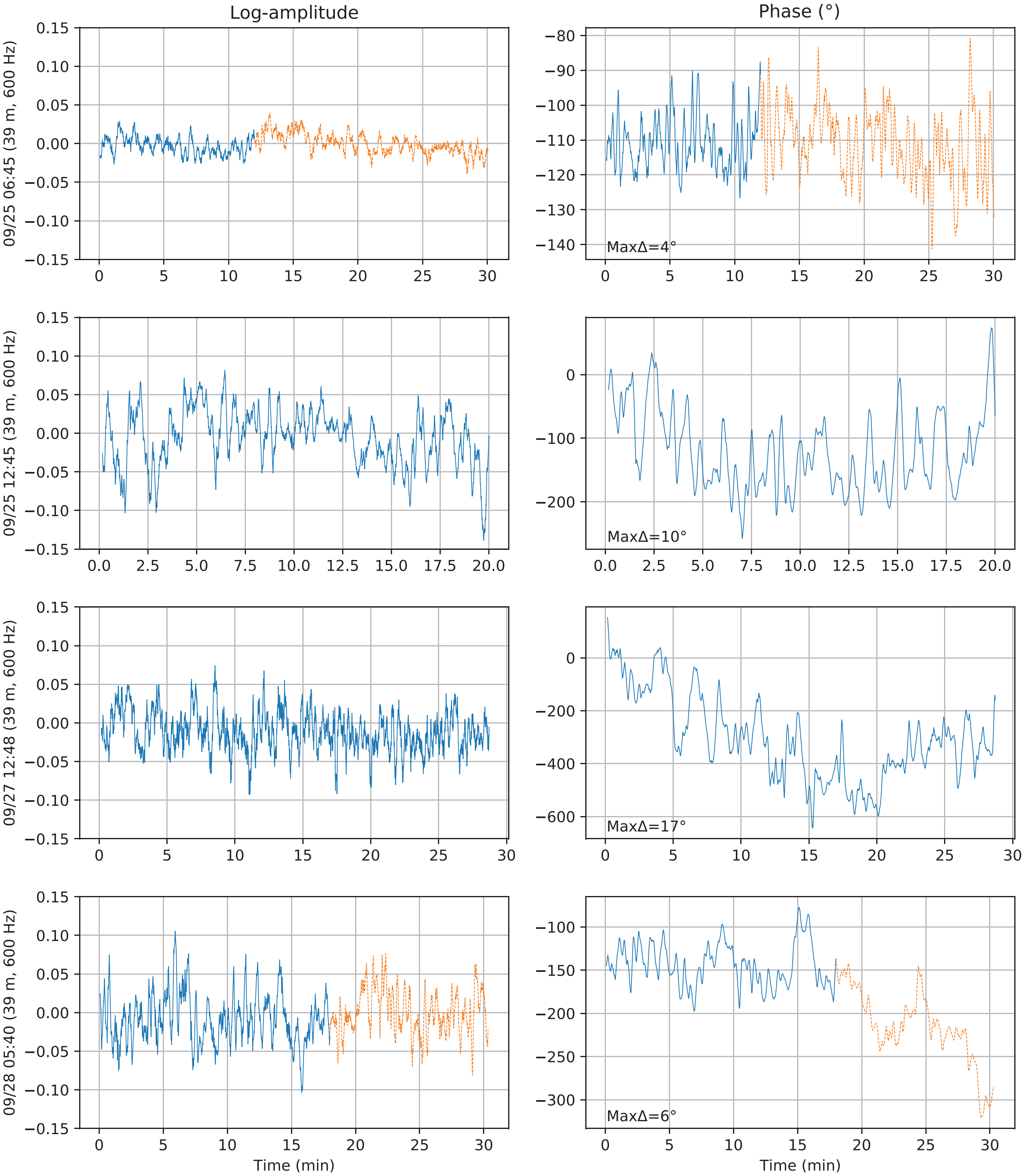

FIG. 10. (Color online) Log-amplitude and phase versus time smoothed using a 10-s moving average for the four selected trials at 39 m and 600 Hz. The subplots with two colors and line styles show the data before (blue, solid) and after (orange, dashed) the vertical dotted lines in Figs. 5 and 8. The log-amplitude scales are the same for all four trials, but the phase scales are different to highlight the fluctuations.

ST predictions. It follows from Fig. 12 that $\sigma_\chi^2$ increases with increasing frequency and height and is in the range 0.001–1. (See SuppPub1.pdf for the log-amplitude variance data from all 16 trials.[25])

The log-amplitude variances measured with the three microphones at the same height are expected to be about the same. For the most part, this is the case for slanted propagation; see the last two rows in Fig. 12 and the supplementary material SuppPub1.pdf.[25] For vertical propagation (the first two rows in Fig. 12 and SuppPub1.pdf),[25] the log-amplitude variances measured with the three microphones deviate significantly, especially for $h = 130\,\mathrm{m}$ and low frequencies, probably because of sound scattering from the tower. Combining this result with the Fresnel zone analysis

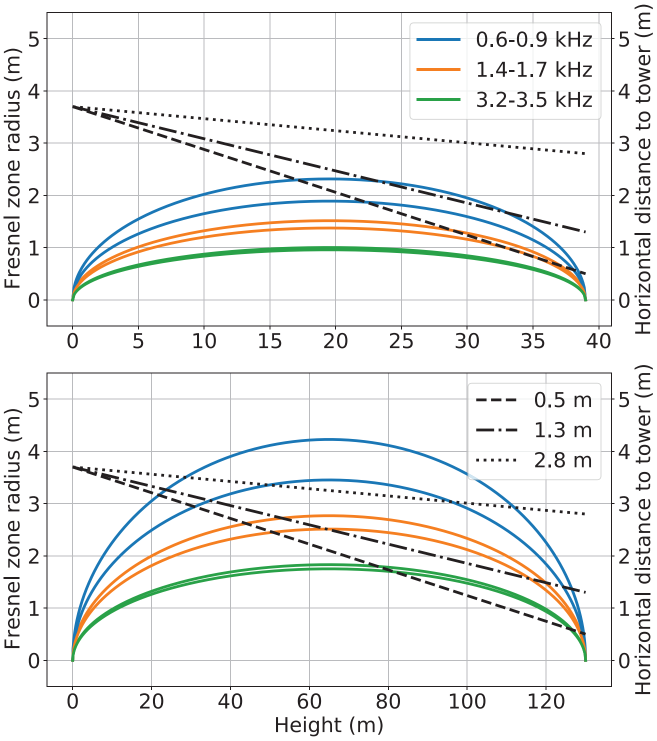

FIG. 11. (Color online) Radius of the first Fresnel zone versus height along the vertical propagation path. Each colored curve represents a different frequency. The dashed, dash-dotted, and dotted lines give the horizontal distances between the tower and the propagation paths to microphones at 0.5 m, 1.3 m, and 2.8 m from the tower, respectively. The upper and lower subplots correspond to microphones at $h = 39$ m and $h = 130$ m.

(Sec. IV D), we conclude that for vertical propagation, the microphones at 2.8 m provide the most accurate log-amplitude measurements, which likely have been affected by tower scattering only at $h = 130$ m and the 600 Hz frequency range.

The log-amplitude fluctuations are affected mainly by the turbulent eddies with sizes on the order of the first Fresnel zone radius $r_F$, Eq. (13). Equation (13) also applies to slanted propagation if $h$ is replaced with the path length $L$ and $z$ with the distance along the path. It follows from Fig. 11 that in the experiment, these eddies were less than about 4 m. For the most part, such eddies are in the inertial subrange of turbulence and are isotropic. Therefore, the experimental results for the log-amplitude variance are expected to agree with the BST predictions.

It follows from Fig. 12 that for the trial on 09/25 at 06:45, the theoretical results underpredict the measured variances in the 1 and 3 kHz ranges. This trial was conducted in a weakly stable ABL for which the turbulence model may not be applicable (Sec. II B). The BST and ST predictions coincide because $Q_H$ is negative (Table I), therefore, $\langle w'T'\rangle$ is set to zero. For 600 Hz and the microphone at heights 130 m and 0.5 m from the tower (the most extreme case), the tower is deep in the first Fresnel zone (Fig. 11), which could explain the large discrepancy between the experiment and the theory.

For the trial on 09/25 at 12:45 (and microphone at 2.8 m from the tower) and the trial 09/27 at 12:48, conducted in unstable ABLs, the measured log-amplitude variances agree relatively well with the BST predictions. The ST theoretical results underpredict the variances.

For 09/28 at 05:40 and observations at 39 m, the BST and ST predictions are close to each other because the surface heat flux is small. These predictions agree with the experimental results. However, at 130 m, the BST results overpredict the measured variances. This can be explained by findings in Secs. IV A–IV C: for the considered trial, the air was more turbulent at 15 m above the ground than at 61 m and higher.

Figure 13 is similar to Fig. 12 but presents results for the phase variance, $\sigma_\phi^2$. It follows from Fig. 13 and SuppPub1.pdf,[25] where the data for all 16 trials are presented, that the phase variances are similar for the three microphones at the same height because the phase fluctuations are caused by eddies that are much larger than the structural elements of the tower (e.g., crossbars of order 1 m), minimizing their effects on the phase variance. For the first three trials in Fig. 13, the phase is unwrapped correctly only for the 600 Hz and (in some cases) 1 kHz ranges. Similar to the log-amplitude, the phase variance increases with increasing frequency and height above the ground. As expected, $\sigma_\phi^2$ is significantly greater than $\sigma_\chi^2$ and in the range 0.05–30 rad$^2$ in Fig. 13 (and up to 100 rad$^2$ in the supplementaary material[25]). The BST and ST results predict even greater phase variances, which were not observed experimentally due to the phase unwrapping issue.

For the trials on 09/25 at 06:45 and 09/28 at 05:40, Fig. 13 indicates that the BST and ST models overpredict the observed phase variances. For the other trials, the measured phase variance tends to agree better with the ST predictions rather than with the BST predictions.

### F. Log-amplitude and phase variances for all trials

Figure 14 depicts the measured log-amplitude and phase variances, $\sigma_\chi^2$ and $\sigma_\phi^2$, versus the BST and ST predictions for all 16 trials. To avoid sound scattering by the tower, the experimental results only include the variances measured at the microphone 2.8 m from the tower. Different colors and symbols specify the trials conducted in different meteorological conditions and with vertical/slanted propagation. The phase subplots have fewer points because the phase could not be unwrapped in many cases. In Fig. 14, the dashed lines show the ideal where the measured and predicted variances are equal. The points above the dashed line indicate that the measured variance is larger than the predicted variance and vice versa.

Figure 14 suggests that the measured log-amplitude variances agree better with the BST predictions than with the ST predictions. On the other hand, the measured phase variances agree better with the ST predictions. These qualitative observations are quantified by calculating the relative

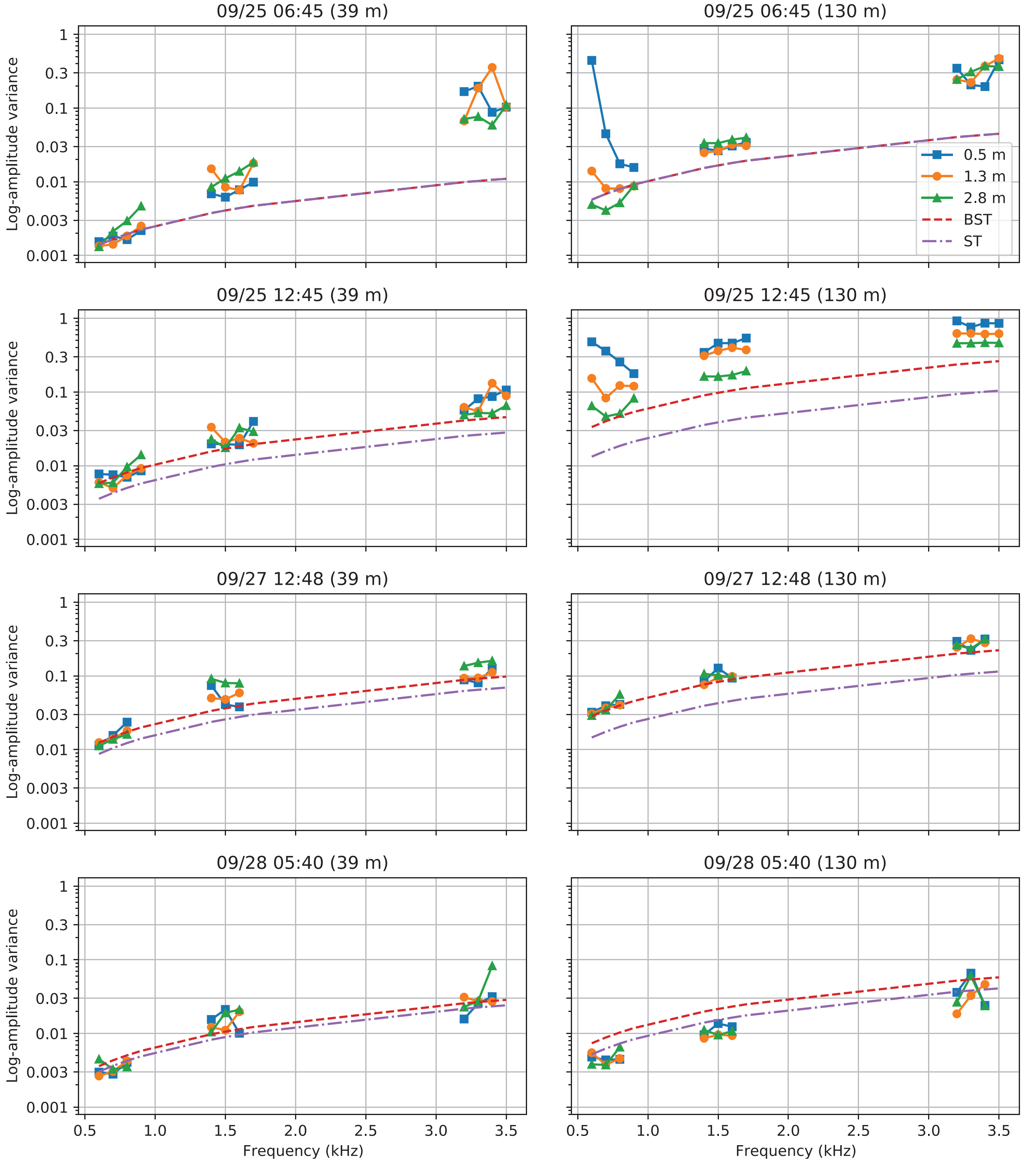

FIG. 12. (Color online) Log-amplitude variance versus frequency for the four selected trials at 39 m and 130 m. The blue squares, orange circles, and green triangles respectively give the experimental results for microphones on the same boom 0.5 m, 1.3 m, and 2.8 m from the tower. The red dashed and purple dash-dotted lines respectively provide the buoyancy-shear-temperature (BST) and shear-temperature (ST) theoretical predictions.

errors between experimental results and theoretical predictions

$$\Delta\sigma^2 = \frac{\sigma_{\rm th}^2 - \sigma_m^2}{\sigma_m^2}. \tag{14}$$

Here, $\sigma_m^2$ is the measured log-amplitude or phase variance, whereas $\sigma_{\rm th}^2$ is the BST or ST theoretical prediction. Table II summarizes the statistical analysis of the relative errors, excluding trials 09/25 at 06:45 (weakly stable case) and 09/27 at 09:06 and 10:01 (tower upwind of the propagation path or meteorological instruments). For the log-amplitude variance, the data with the measured $\sigma_\chi^2 > 0.2$ are also excluded because such data correspond to strong scattering, whereas Eq. (4) is valid for weak scattering. In Table II, a positive bias indicates that, on average, the BST or ST

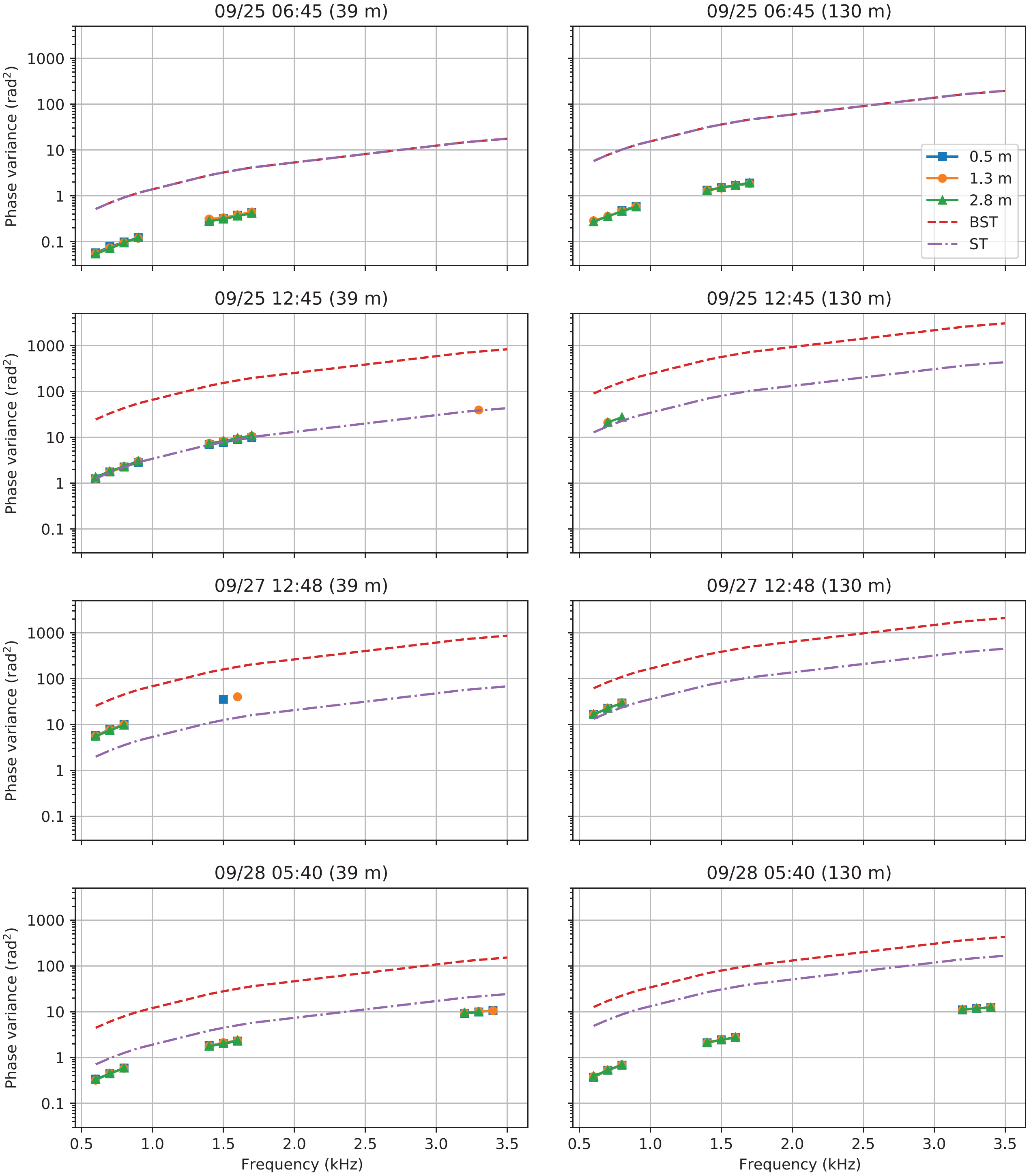

FIG. 13. (Color online) Details are the same as in Fig. 12 but for the phase variance versus frequency.

prediction is greater than what was measured, which corresponds to a symbol that is below the dashed lines in Fig. 14.

Table II demonstrates that the magnitudes of the log-amplitude biases are smaller for the BST predictions than they are for the ST predictions. The BST bias for 9/28 is 0.13, while that for other slanted trials is about twice as large in magnitude and opposite in sign. The vertical propagation has a larger bias magnitude, likely due to sound scattering by the tower. For BST predictions, excluding the 09/28 trials, the standard deviations of the relative errors for the log-amplitude variances are about 0.2. Such standard deviations are typical for measurements involving turbulence. For the trials on 09/28, the standard deviation is about twice as large (0.5), probably due to an evolving meteorological regime of that day. As we did not apply any tests for non-stationarity,[26] some of the trials might not have been conducted in a fully developed, stationary ABL for which the turbulence model in Sec. II B applies. This possible

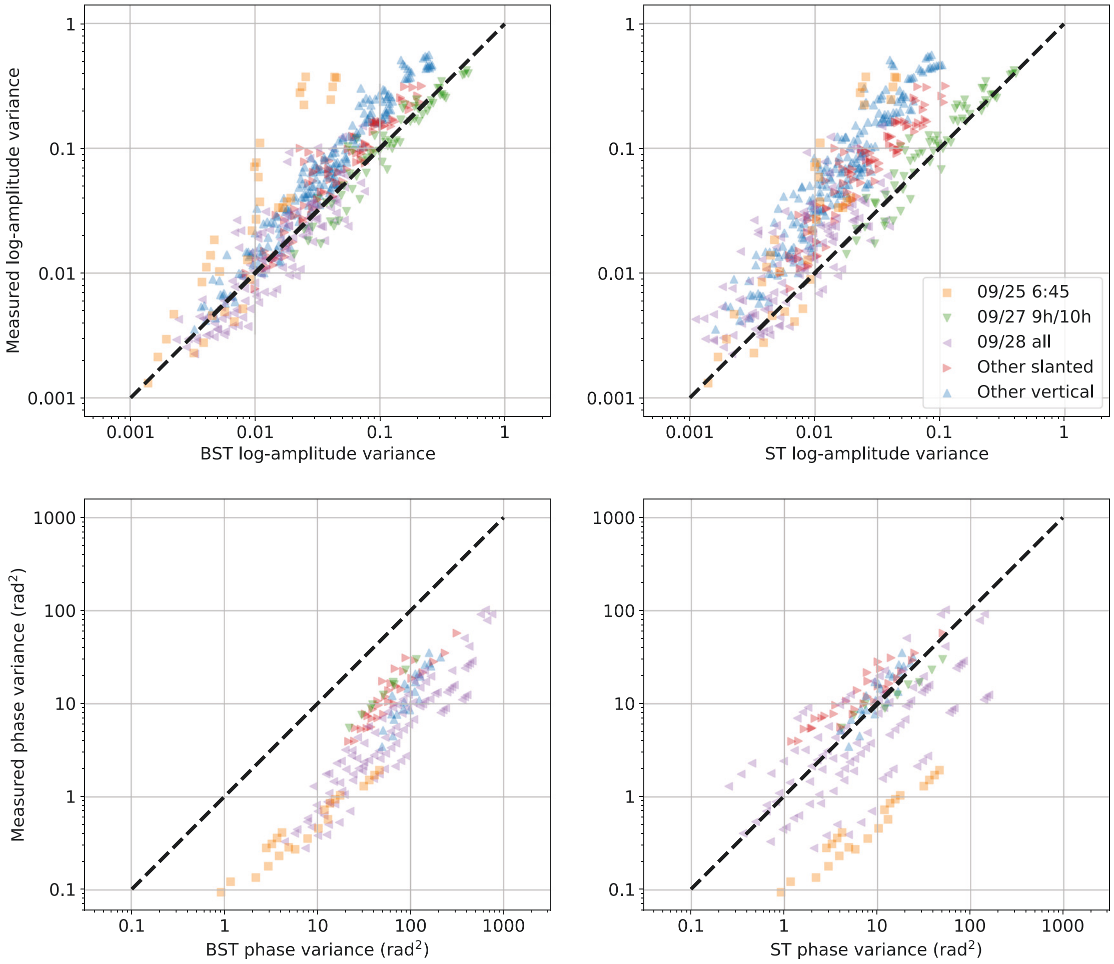

FIG. 14. (Color online) Measured log-amplitude and phase variances versus the BST and ST theoretical predictions. The orange squares are for the trial on 09/25 at 06:45 (a weakly stable ABL), the green downward-pointing triangles are for the trials 09/27 at 09:06 and 10:01 (a tower wake issue), the red right-pointing triangles are for the other trials on 09/27 with slanted propagation, the violet left-pointing triangles are for all trials on 09/28 (low-wind and cloudy), and the blue upward-pointing triangles are for all trials on 09/28 (low-wind and cloudy), and the blue up triangles are for all other trials with vertical propagation.

deviation from the model assumptions may also partially explain the increased standard deviations (and biases).

For the phase variance, the bias magnitudes are much smaller for the ST predictions than they are for the BST predictions. The phase standard deviations follow a pattern similar to that of the log-amplitude standard deviations with the 09/28 trials showing the greater spread.

TABLE II. Bias and standard deviation (Std. Dev.) of the relative error, and $N$ is the number of samples.

| Relative error | | Log-amplitude variance | | | Phase variance | | |
|---|---|---|---|---|---|---|---|
| Trial | Model | $N$ | Bias | Std. Dev. | $N$ | Bias | Std. Dev. |
| Other vertical | BST | 157 | −0.34 | 0.20 | 23 | 7.01 | 2.76 |
| Other vertical | ST | 157 | −0.68 | 0.13 | 23 | −0.15 | 0.26 |
| Other slanted | BST | 72 | −0.25 | 0.23 | 31 | 4.02 | 1.17 |
| Other slanted | ST | 72 | −0.58 | 0.15 | 31 | −0.45 | 0.20 |
| 09/28 all | BST | 117 | 0.13 | 0.49 | 105 | 14.13 | 7.54 |
| 09/28 all | ST | 117 | −0.34 | 0.39 | 105 | 1.91 | 3.46 |

Table II substantiates that the theory in Eqs. (4)–(7) can be used to predict the log-amplitude variances, which are affected by small-scale isotropic turbulence. The measured phase variances agree better with the ST theoretical predictions. This insight can lead to future development of a turbulence model that accounts for the largest anisotropic eddies being blocked by the ground.

## V. CONCLUSIONS

This article presented experimental data with comparison to theoretical predictions for log-amplitude and phase fluctuations of narrowband acoustic signals propagating over vertical and slanted paths in the near-ground turbulent atmosphere.

Existing theoretical formulations for the variances of the log-amplitude and phase fluctuations were outlined. The pertinent turbulence model provided the height-dependent variances and length scales of the temperature fluctuations and the buoyancy- and shear-produced velocity fluctuations. The limitations of this isotropic model were discussed and approaches were suggested to generalize the model for anisotropic turbulence.

An experiment on vertical and slanted sound propagation conducted at the NWTC was described. The main feature of the experiment was to place microphones on three horizontal booms mounted to the 135-m meteorological tower at different heights. A ground-based speaker transmitted narrowband tones and was either immediately below the microphones or at some distance from the tower.

Acoustic recordings were processed into time series of the amplitudes and phases of the tones for all experimental trials. For the four selected trials, phasor scatterplots exhibit the full spectrum of scattering behavior: unsaturated, partially saturated, and fully saturated. Three of the trials exhibited an increase in the amplitude and phase fluctuations with increasing height, whereas the fourth had a decrease with height, which might be explained by turbulence concentrating below a low-level jet combined with the slanted geometry of the propagation path.

Finally, the relative errors between the measured log-amplitude and phase variances and the BST or ST theoretical predictions were analyzed. The former predictions are based on the turbulence model employed in the article, whereas the latter omit the buoyancy-produced velocity fluctuations. The measured log-amplitude variances agree relatively well with the BST predictions as would be expected as the amplitude fluctuations are caused by small-scale isotropic turbulence, which is described correctly by the existing turbulence model. However, the BST theoretical results significantly overpredict the variance of the phase fluctuations, which are caused by large anisotropic eddies. Somewhat surprisingly, the measured phase variances agree relatively well with the ST predictions. This result suggests that the turbulence model should be modi-fied to account for the ground blocking large eddies.

In future work, we plan to examine other statistical characteristics of acoustic signals such as statistics of pulse propagation; distributions of signals at one or multiple points in space, time, or frequency; and the spatial, temporal, and cross-frequency coherences.

Supplemental material is available at
https://doi.org/10.1121/10.0003820
under the "Supplemental" tab.

## REFERENCES

[1] K. Attenborough, K. M. Li, and K. Horoshenkov, *Predicting Outdoor Sound* (Taylor and Francis, London, England, 2006), p. 441.

[2] E. M. Salomons, *Computational Atmospheric Acoustics* (Springer, Dordrecht, The Netherlands (2001), pp. 181–202.

[3] V. E. Ostashev and D. K. Wilson, *Acoustics in Moving Inhomogeneous Media* (CRC Press, Boca Raton, FL, 2016), p. 541.

[4] S. Cheinet, M. Cosnefroy, F. Königstein, W. Rickert, M. Christoph, S. L. Collier, A. Dagallier, L. Ehrhardt, V. E. Ostashev, A. Stefanovic, T. Wessling, and D. K. Wilson, "An experimental study of the atmospheric-driven variability of impulse sounds," J. Acoust. Soc. Am. **144**(2), 822–840 (2018).

[5] B. G. Ferguson and K. W. Lo, "Acoustic detection, localization, and tracking of tactical autonomous aerial and underwater vehicles," J. Acoust. Soc. Am. **140**(4), 3119 (2016).

[6] G. H. Goldman, "Acoustic detection results for a small unmanned aircraft system extrapolated over range," J. Acoust. Soc. Am. **140**(4), 3120 (2016).

[7] V. E. Ostashev, M. V. Scanlon, D. K. Wilson, and S. N. Vecherin, "Source localization from an elevated acoustic sensor array in a refractive atmosphere," J. Acoust. Soc. Am. **124**(6), 3413–3420 (2008).

[8] P. H. Parkin and W. E. Scholes, "Air–to–ground sound propagation," J. Acoust. Soc. Am. **26**(6), 1021–1023 (1954).

[9] P. K. Kasper, R. S. Pappa, L. R. Keefe, and L. C. Sutherland, "A study of air-to-ground sound propagation using an instrumented meteorological tower," NASA CR-2617, National Aeronautics and Space Administration, Washington, D.C. (1975), available at ntrs.nasa.gov/archive/nasa/casi.ntrs.nasa.gov/19760003267.pdf (Last viewed 23 October 2020) as prepared by Wyle Laboratories, Hampton, VA.

[10] P. Blanc-Benon, B. Lipkens, L. Dallois, M. F. Hamilton, and D. T. Blackstock, "Propagation of finite amplitude sound through turbulence: Modeling with geometrical acoustics and the parabolic approximation," J. Acoust. Soc. Am. **111**(1), 487–498 (2002).

[11] T. A. Stout and V. Sparrow, "Statistics of supersonic signatures propagated through simulated atmospheric turbulence," J. Acoust. Soc. Am. **141**(5), 3729 (2017).

[12] F. Coulouvrat, D. Luquet, and R. Marchiano, "Numerical model of sonic boom in 3D kinematic turbulence," AIP Conf. Proc. **1685**(1), 090008 (2015).

[13] F. Rietdijk, J. Forssén, and K. Heutschi, "Generating sequences of acoustic scintillations," Acta Acust. Acust. **103**(2), 331–338 (2017).

[14] V. E. Ostashev and D. K. Wilson, "Statistical characterization of sound propagation over vertical and slanted paths in a turbulent atmosphere," Acta Acust. Acust. **104**(4), 571–585 (2018).

[15] L. C. Sutherland and G. A. Daigle, "Atmospheric sound propagation," in *Handbook of Acoustics*, edited by M. J. Crocker (Wiley, Hoboken, NJ, 1998), Chap. 28, pp. 305–329.

[16] N. N. Zernov and V. E. Gherm, "Strong scintillation of GNSS signals in the inhomogeneous ionosphere: 1. Theoretical background," Radio Sci. **50**(2), 153–167, https://doi.org/10.1002/2014RS005603 (2015).

[17] V. E. Ostashev, D. K. Wilson, S. N. Vecherin, and S. L. Collier, "Spatial-temporal coherence of acoustic signals propagating in a refractive, turbulent atmosphere," J. Acoust. Soc. Am. **136**(5), 2414–2431 (2014).

[18] S. M. Rytov, Y. A. Kravtsov, and V. I. Tatarskii, *Principles of Statistical Radiophysics 4: Wave Propagation through Random Media* (Springer, Berlin, Germany, 1989), p. 188, translated from Russian by A. P. Repyev.

[19] J. C. R. Hunt, "Turbulence structure in thermal convection and shear-free boundary layers," J. Fluid Mech. **138**, 161–184 (1984).

[20] D. K. Wilson, "A three-dimensional correlation/spectral model for turbulent velocities in a convective boundary layer," Boundary-Layer Meteorol. **85**, 35–52 (1997).

[21] V. E. Ostashev and D. K. Wilson, "Non-Markov character of the phase fluctuations for sound propagation over relatively small ranges in the turbulent atmosphere," J. Acoust. Soc. Am. **145**(6), 3359–3369 (2019).

[22] National Wind and Technology Center, available at nrel.gov/nwtc/ (Last viewed 23 October 2020).

[23] M. Sadoud, "Lattice tower shadow effect investigation," Technical Note 800113-CAMO-T-01, GL Garrad Hassan Canada, Inc., Ottawa, Ontario (2012), available at wind.nrel.gov/MetData/Publications/800113-CAMO-T01-C-NREL\%20Tower\%20Shadow_FINAL.pdf (Last viewed 23 October 2020).

[24] R. B. Stull, *An Introduction to Boundary Layer Meteorology* (Springer, Dordrecht, The Netherlands, 1988), p. 666.

[25] See supplementary material at https://www.scitation.org/doi/suppl/10.1121/10.0003820 for the log-amplitude and phase variances versus frequency (similar to Figs. 13 and 14) for all 16 trials.

[26] X. Lee, W. Massman, and B. Law, *Handbook of Micrometeorology: A Guide for Surface Flux Measurement and Analysis* (Springer, Dordrecht, The Netherlands, 2004), p. 181–208.

# REPORT DOCUMENTATION PAGE

*Form Approved*
*OMB No. 0704-0188*

| | | |
|---|---|---|
| **1. REPORT DATE** ***(DD-MM-YYYY)***<br>May 2021 | **2. REPORT TYPE**<br>Final | **3. DATES COVERED** ***(From - To)*** |
| **4. TITLE AND SUBTITLE**<br>Vertical and Slanted Sound Propagation in the Near-Ground Atmosphere: Amplitude and Phase Fluctuations | | **5a. CONTRACT NUMBER**<br>**5b. GRANT NUMBER**<br>**5c. PROGRAM ELEMENT NUMBER**<br>611102A |
| **6. AUTHOR(S)**<br>Matthew J. Kamrath, Vladimir E. Ostashev, D. Keith Wilson, Michael J. White, Carl R. Hart, and Anthony Finn | | **5d. PROJECT NUMBER**<br>T24<br>**5e. TASK NUMBER**<br>01<br>**5f. WORK UNIT NUMBER** |
| **7. PERFORMING ORGANIZATION NAME(S) AND ADDRESS(ES)**<br>See next page. | | **8. PERFORMING ORGANIZATION REPORT NUMBER**<br>ERDC MP-21-2 |
| **9. SPONSORING / MONITORING AGENCY NAME(S) AND ADDRESS(ES)**<br>U.S. Army Corps of Engineers<br>Washington, DC 20314 | | **10. SPONSOR/MONITOR'S ACRONYM(S)**<br>**11. SPONSOR/MONITOR'S REPORT NUMBER(S)** |

**12. DISTRIBUTION / AVAILABILITY STATEMENT**

Approved for public release; distribution is unlimited.

**13. SUPPLEMENTARY NOTES**

This article was originally published online in the *Journal of the Acoustical Society of America* on 26 March 2021.

**14. ABSTRACT**

Sound propagation along vertical and slanted paths through the near-ground atmosphere impacts detection and localization of low-altitude sound sources, such as small unmanned aerial vehicles, from ground-based microphone arrays. This article experimentally investigates the amplitude and phase fluctuations of acoustic signals propagating along such paths. The experiment involved nine microphones on three horizontal booms mounted at different heights to a 135-m meteorological tower at the National Wind Technology Center (Boulder, CO). A ground-based loudspeaker was placed at the base of the tower for vertical propagation or 56 m from the base of the tower for slanted propagation. Phasor scatterplots qualitatively characterize the amplitude and phase fluctuations of the received signals during different meteorological regimes. The measurements are also compared to a theory describing the log-amplitude and phase variances based on the spectrum of shear and buoyancy driven turbulence near the ground. Generally, the theory correctly predicts the measured log-amplitude variances, which are affected primarily by small-scale, isotropic turbulent eddies. However, the theory overpredicts the measured phase variances, which are affected primarily by large-scale, anisotropic, buoyantly driven eddies. Ground blocking of these large eddies likely explains the overprediction.

**15. SUBJECT TERMS**

Sound—Detection, Boundary layer (Meteorology), Microphone arrays, Drone aircraft

| | | | | | |
|---|---|---|---|---|---|
| **16. SECURITY CLASSIFICATION OF:** | | | **17. LIMITATION OF ABSTRACT** | **18. NUMBER OF PAGES** | **19a. NAME OF RESPONSIBLE PERSON** |
| **a. REPORT**<br>Unclassified | **b. ABSTRACT**<br>Unclassified | **c. THIS PAGE**<br>Unclassified | SAR | 24 | **19b. TELEPHONE NUMBER** ***(include area code)*** |

**Standard Form 298 (Rev. 8-98)**
**Prescribed by ANSI Std. 239.18**

**7. PERFORMING ORGANIZATION NAME(S)**

U.S. Army Engineer Research and Development Center
Cold Regions Research Laboratory
72 Lyme Road
Hanover, NH 03755

U.S. Army Engineer Research and Development Center
Construction Engineering Laboratory
2902 Newmark Drive
Champaign, IL 61822

Defence and Systems Institute
University of South Australia
Mawson Lakes, SA 5095, Australia